

A Heterostructured Sulfonated CNT/Sulfur/CNT Cathode for Promoting the Binary Conversion of Polysulfides in Lithium-Metal Batteries

Min Li,^[a, c] Xianxian Zhou,*^[a] Xiaoxiao Liu,^[a] Liang Chen,^[a] Ding Zhang,^[a] Shoudong Xu,^[a] Donghong Duan,^[a] Qinbo Yuan,^[b] Lixia Ling,*^[a] and Shibin Liu*^[a]

The shuttle effect of lithium polysulfides (LiPS) and sluggish redox kinetics hinder the commercialization of lithium-sulfur (Li–S) batteries. Herein, we design a lightweight and multifunctional multi-walled carbon nanotube (CNT)/sulfur/lithiated sulfonated CNT (M/S/M-SO₃Li) electrode as energy storage devices. Flexible CNT films ensure continuously electron/ion transmission and serve as LiPS shielding layer. Moreover, guided by DFT and experimental results, SO₃⁻ groups exert a vital adsorption effect toward sulfur species but not NH₄⁺ groups.

The SO₃⁻ groups can not only employ as LiPS immobilizer by Li–O bands between LiPS and SO₃⁻, but also serve as multifunctional electrocatalyst to propel LiPS conversion via generating thiosulfate and polythionate and Li₂S decomposition by reducing reaction overpotential. As expected, M/S/M-SO₃Li electrode exhibits prominent rate capability (723.5 mAh g⁻¹ at 5 C), high sulfur loading (7.09 mAh cm⁻² at 5.0 mg cm⁻² sulfur), favorable anti-self-discharge capabilities (rest for 72 h at 0.5 C with 2.17%).

1. Introduction

With the development of technology, lithium-ion batteries have been unable to meet the demand for high-energy-density secondary batteries such as portable electronic products and electric vehicles.^[1,2] Li–S battery is one of the promising candidates for the next-generation energy storage systems due to its high theoretical energy density (2600 Wh kg⁻¹), theoretical specific capacity (1675 mAh g⁻¹), environmental friendliness, low cost and earth-abundance sulfur material.^[3–6] However, there are still multiple obstacles leading to poor cycle stability and rate performance, which inhibits the commercialization of Li–S battery.^[7,8] They are mainly reflected in the following aspects: i) the inherent insulation of sulfur cathode and its reduction products Li₂S/Li₂S₂, which induces low electron transport rate and the utilization of the sulfur species. ii) The shuttle effect of soluble LiPS intermediates in the electrolyte, leading to poor Coulombic efficiency. iii) The growth of Li dendrite and

the nonuniform deposition of Li₂S, which results in safety issues and fast capacity fading.^[9–12]

However, the shuttle effect of LiPS and sluggish redox dynamics are recognized as the main factors affecting the cycling stability and rate performance among the aforementioned obstacles. Hence, considerable promotion strategies have been explored to modify the cathode to overcome these challenges facing Li–S batteries.^[13–15] These strategies can be summarized as either physical confinement,^[16–18] chemisorption,^[19–21] electrostatic repulsion^[22,23] or catalyst conversion effects.^[24–26] Although confinement and anchoring strategies can efficiently prevent the LiPS shuttle and synchronously improve the cycling stability and rate capability, they are fundamentally incapable of tackling the irreversible loss of LiPS, which will unavoidably lead to low sulfur utilization and rapid capacity loss. In this regard, the design of electrocatalysts with catalyst conversion effects has attracted considerable interest on account of its remarkable physiochemical and electrocatalytic effects for LiPS.

Although the catalyst conversion approach can simultaneously address the LiPS shuttle and sluggish reaction kinetics, current research strategies in Li–S batteries have been devoted to designing electrocatalysts with high catalytic activity. This has typically been achieved through the development of metal compounds (metal oxides,^[27–30] sulfides,^[31–34] nitrides^[35,36] and phosphides^[37,38]), which still present significant disadvantages, such as toxicity (H₂S and H₃P), the need for precise structural control, excess weight and volume and so on. Lightweight plays an indispensable role for orientating toward the high-energy-density advantages of Li–S batteries. Therefore, to realize high-energy-density Li–S batteries, there is a necessity for lightweight electrocatalysts, meaning that metal compounds are not optimal. Usually, catalysts are supported on a lightweight carbon matrix to construct a hybrid cathode,

[a] M. Li, Dr. X. Zhou, X. Liu, Dr. L. Chen, Dr. D. Zhang, Dr. S. Xu, Dr. D. Duan, Dr. L. Ling, Prof. Dr. S. Liu
School of Taiyuan University of Technology
College of Chemistry and Chemical Engineering
Taiyuan 030024, China
E-mail: zhouxianxian@tyut.edu.cn
linglixia@tyut.edu.cn
sbliu@tyut.edu.cn

[b] Dr. Q. Yuan
Debrider and Ecological Engineering Technology Co., Ltd. Institution
Taiyuan 030031, China

[c] M. Li
Dalian Institute of Chemical Physics
Dalian National Laboratory for Clean Energy
Chinese Academy of Sciences
Dalian 116023, China

 Supporting information for this article is available on the WWW under
<https://doi.org/10.1002/batt.202100302>

particularly for tightly self-assembled nanosized carbon matrices, which is a feasible approach to further improve the electrochemical performance and energy density.

Accordingly, extensive research has proved that polar functional groups, such as sulfonic, amino and phosphate groups, decorated on carbon substrates demonstrate potential as lightweight catalysts in comparison to carbon loading metal catalysts in further improving the electrochemical performance of Li–S batteries.^[39–41] For example, Fretz et al. demonstrated lithium sulfonate groups attached to ordered mesoporous carbon (LiSO₃-CMK3) with a 0.32 mmol g⁻¹ sulfonate loading resulting in reduced LiPS shuttling and can be possibly used as an immobilized cathode instead of LiNO₃.^[42] Furthermore, Wang et al. studied the introduction of different functional groups in Ti₃C₂ MXenes and found that S and O are the best choices for the adsorption capacity of Ti₃C₂T₂ to polysulfides and the electrocatalytic performance of Li₂S.^[43] Generally, due to their cross-linked and compact structures, nanosized carbon matrices intrinsically possess high density. Inspired by this, Sun et al. proposed a novel lightweight strategy by combining benzene functional groups with N/O and S/O groups and directly grafted them on an expanded reduced graphene oxide surface with a closely packed nanosized structure, thereby improving the practical energy and power densities of Li–S cells.^[44] Hence, methods for constructing three-dimensional (3D) interconnected and closely packed carbon skeletons as sulfur host matrices and polar functional groups as electrocatalysts are crucial for realizing higher energy density Li–S batteries.

In addition to lightweight, multifunctionality is of equal importance for directly impacting the commercial applications of Li–S batteries. Multifunctionality only reduces the reaction overpotential and chemically adsorb sulfur species but also accelerates Li⁺ transport and retards the diffusion of negatively polysulfides together with rapid catalytic conversion. Several designed cathodes with lightweight properties have been shown to considerably improve the electrochemical performance of Li–S batteries, with most of them only synergistically exploiting one or two of above strategies. For example, Jia et al. reported a g-C₃N₄/S hybrid cathode with a high N doping content and high absorptivity, thereby further suppressing the shuttle effect of polysulfides through its excellent chemical adsorption ability and improving the rate performance of Li–S batteries.^[45] Mo et al. prepared a hollow sulfur nanocrystal supported on graphene nanosheets as a cathode, which formed a space confinement for inhibiting polysulfide migration and displayed a remarkable rate performance and superior cycling stability.^[46] Although these approaches solved the shuttle effect of polysulfides through chemical adsorption or physical limitations, they failed to transform and accelerate the transmission of Li⁺ ions and other multifunctional effects of reducing battery polarization.

By contrast, to achieve integration with multiple functions, it is necessary to meet the requirements via the addition of the corresponding functional materials. However, this inevitably increases the internal resistance and decreases the energy density of the cells when introducing multicomponents. For example, Chen et al. fabricated a multifunctional cobalt-

embedded and nitrogen-doped carbonaceous microflower as a sulfur host. This not only restrained the LiPS shuttle via the synergy of physical capture and strong chemisorption but also facilitated the conversion of soluble polysulfides.^[47] Consequently, it is attractive to rationally design a novel cathode that can effectively restrain LiPS shuttling and boost the sulfur species reaction kinetics, especially for the LiPS reduction and Li₂S oxidation processes, as well as to exert a multifunctional synergistic effect to improve the overall performance of Li–S batteries only by a single or few component modifications.

Inspired by the above considerations, a 3D flexible self-supporting CNT matrix is designed here that provides ample exposed sites for regulating isolated Li₂S stripping with 3D porous cross-linking channels and improved interfacial contact, thereby ensuring long-range electron/ion transport network. Meanwhile, polar SO₃ groups can block LiPS by the formation of Li–O bonds between LiPS and SO₃ and catalyze the conversion kinetics of LiPS and Li₂S, as evidenced by density functional theory (DFT) calculations. Moreover, due to rapid Li⁺ diffusion, it is also favorable to control the homogenous nucleation and reduce the decomposition barrier of Li₂S during cycling, thus avoiding the formation of irregular lithium dendrites. Based on the above outstanding characteristics, the integrated M/S/M-SO₃Li electrode displays remarkable cycling stability, high-rate capability and ultra-long lifespan. Furthermore, the M/S/M-SO₃Li electrode with high sulfur loading still maintains an excellent reversible areal capacity of 7.09 mAh cm⁻².

2. Results and Discussion

2.1. Characterization of M/S/M-SO₃Li

The schematic diagram of M/S/M-SO₃Li electrode is illustrated in Figure 1(a), which was synthesized by a facile approach. Detailed synthesis procedure can be presented in experimental process. The CNTs/S composite was synthesized via a melt-diffusion method. Afterward, the CNTs-SO₃Li was coated onto three-dimensional (3D) conductive network, assembling the electrode material of M/S/M-SO₃Li.

To confirm the successfully grafted of sulfonic acid group, FTIR and XPS of CNTs-SO₃Li were performed. Figure S1(a) shows typical absorption peaks at 1024.8 and 1094.8 cm⁻¹, corresponding to the symmetric and asymmetric stretching vibration of S–O bond.^[48,49] Meanwhile, the existence of S2p spectra with characteristic peaks centered at 168.7 and 169.9 eV, are assigned to S–O bond (Figure S1b).^[50,51] Raman spectroscopy was further performed to confirm the chemical structure of CNTs, and CNTs-SO₃Li, as shown in Figure 1(b). The presence of two peaks at 1364 cm⁻¹ for D band and 1619 cm⁻¹ for G band were distinct, referring to D band and G band.^[22,52] The D band corresponds to sp³-hybridized carbon atoms, being attributed to stretching mode of non-sp²-hybridized carbon and in-plane symmetric stretching vibration of sp²-hybridized carbons.^[53] The I_D/I_G ratio is an important parameter to determine the defect density, disorder, edge smoothness and edge structures. The

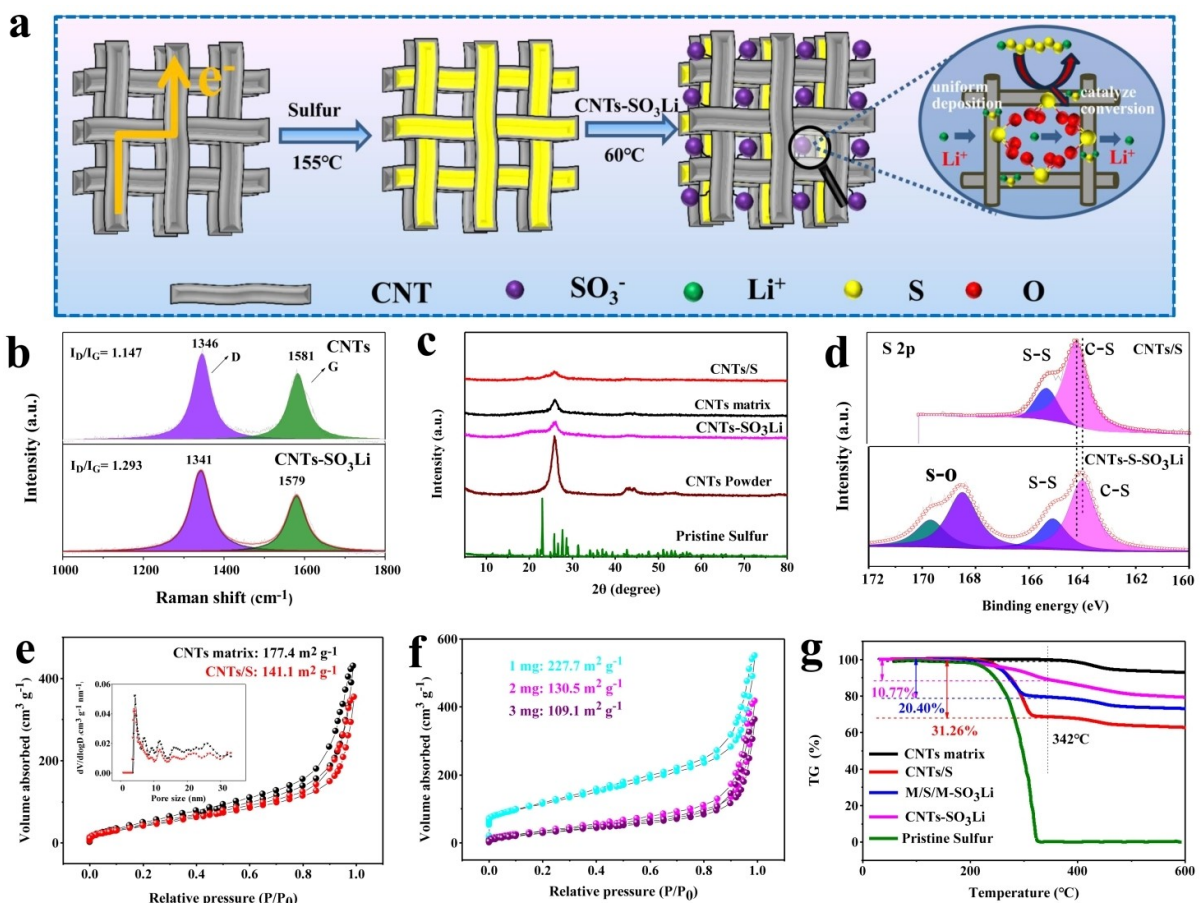


Figure 1. a) Schematic illustration of the synthesis procedure of the M/S/M-SO₃Li electrode. b) Raman spectra of CNTs and CNTs-SO₃Li. c) XRD patterns of pristine sulfur, CNTs powder, self-supporting CNTs, CNTs/S and CNTs-SO₃Li. d) XPS spectra S2p of CNTs/S and CNTs-SO₃Li. Nitrogen adsorption and desorption isotherms e) freestanding CNTs film and CNTs/S, and pore size distribution of CNTs film (inset); f) different contents of CNTs-SO₃Li. g) TG analysis.

I_D/I_G ratio of CNTs-SO₃Li was larger than that of CNTs which increased from 1.147 to 1.293, demonstrating the proportion of D bands in CNTs-SO₃Li increase, which the proportion of G bands decrease. With the grafting of organic functional groups during sulfonation, it coincides well with the result of expectations when the grafting of organic functional groups was successful during sulfonation. It is apparently revealed the formation of SO₃ groups in CNTs.

To investigate the structure evolution process, the X-ray diffraction (XRD) analysis was carried out. As illustrated in Figure 1(c), the XRD pattern of CNTs powder shows a sharp diffraction peak at 26° and a weak peak at 43.04°, reflecting the existence of amorphous carbon and corresponding the (002) and (100) plane of the CNTs, respectively.^[26] By comparison, the XRD of CNTs film, CNTs film with sulfur (CNTs/S) and CNTs-SO₃Li can observe a weaken peak at 26° and 43.04°, originating from the coating effect. Meanwhile, there are no emerging diffraction peaks existing, which mean that impurities are hardly formed during the synthesis process. The position of diffraction peaks didn't appear obvious shift, indicating the intercalation of other substances scarcely changes the spatial distribution and emerging crystal phase. The XRD spectrum of pristine sulfur shows typical peaks at around 15.4°, 23° and 31.4°,

representing the (113), (222) and (044) crystalline structure of orthorhombic sulfur.^[54] For the CNTs/S composite, the sulfur peaks almost disappeared, only a single weak peak at 23°. This result indicates that the externally coated sulfur is amorphous, which is favorable to increase the solubility of sulfur due to the decreased dissolution barrier. To further verify the existence of amorphous sulfur, the XPS of CNTs/S and CNTs-SO₃Li electrode were analyzed in Figure 1d. The spectra of S2p was separated to two peaks at 164.2 and 165.3 eV, corresponding to C-S and S-S bond in CNTs/S electrode.^[55] The emergence of C-S bond is ascribed to S-S bond cleavage of crystalline S₈ and then constructs a new bond with C atoms of CNTs substrate. This result further demonstrates that sulfur presents amorphous state in CNTs/S composite, being consistent with XRD result (Figure 1c). In S2p spectra of CNTs-S-SO₃Li electrode, it also exists C-S and S-S bond, but also appears S-O bond which is attributed to SO₃ groups.

The Nitrogen adsorption/desorption test was performed to analyze surface area and pore distribution. As displayed in Figure 1(e), CNTs matrix presents a Brunauer-Emmett-Teller (BET) surface area of 177.4 m² g⁻¹ with well-fined ~5 nm mesopore, suggesting that it can expose ample contact sites for regulating 3D Li₂S deposition and efficacious immobilizing

LiPS, and enhance sulfur loading and electrolyte permeation for fast electron/ion transport. Notably, with the addition of sulfur components, the surface area of CNTs/S (sulfur loading $\sim 1.5 \text{ mg cm}^{-2}$) decreases to $141.1 \text{ m}^2 \text{ g}^{-1}$, indicating the existence of active sulfur inevitably penetrated into pore structure of CNTs, which presents the enormous potential for high sulfur loading due to mostly residual porosity. To probe the distribution of SO_3 groups in M/S/M- SO_3Li electrode, the surface area with the different loading of SO_3 groups was collected in Figure 1(f). As the amount of SO_3 groups increase, the smaller the surface area is. That is to say, in addition to being distributed on the surface of M/S/M- SO_3Li electrode, the SO_3 groups also exist in porous channels.

TG analysis was conducted for further evaluation of sulfur content on whole electrode. As shown in Figure 1(g), flexible CNTs substrate has no weight loss until 400°C indicating that it possesses excellent thermal stability. Figure 1(g) exhibits the 31.26% and 20.40% weight loss for the CNTs/S and M/S/M- SO_3Li electrodes, respectively. The former is attributed to the evaporation of sulfur, while the latter is ascribed to the decomposition of CNTs- SO_3Li and sulfur loss, which is consistent well with the theoretical content of sulfur on the electrode.

The morphological features were demonstrated by SEM and TEM images, as shown in Figure 2. The free-standing CNTs matrix are shown in Figure 2(a and d), where interconnected CNTs shows a porous network structure and uniformly

distribute 3D wormhole-like morphology, and it is favorable for providing abundant pathways toward fast lithium-ion migration and electron transport. The CNTs matrix was assembled with an average diameter of $\sim 12 \text{ nm}$, observed in insert of Figure 2(a). The CNTs/S composite electrode still remains abundant wormhole-like channels in Figure 2(b and e), which ensures the penetration of the electrolyte and promotes rapid transfer of ions and electrons. Moreover, it is cruder than that of CNTs matrix with an average diameter, demonstrating sulfur element encapsulated successfully into CNTs surface, which can improve the effective utilization rate of sulfur species. Thus, according to the XRD and SEM, the sulfur component can not only confine in the pore structures but embrace on the CNTs surface. In addition, mapping of CNTs/S reveals the existence and homogeneous distribution of C and S element, which ensures better utilization efficiency of sulfur material. Moreover, the content of C is calculated to be 60 wt%, while the content of S is 33 wt% by EDS (Table S1), in agreement with the TG results (Figure 1g). Figure 2(c) exhibits CNTs- SO_3Li uniformly distributes on substrates, rather than aggregates, maintaining 3D-interconnected architecture. Meanwhile, the homogenous lamella embraced closely along the CNTs outside surface is observed from TEM in Figure 2f, further proving SO_3 groups were successfully grafted on the CNTs surface, coincided with FTIR, XPS and TG analysis. From the profiles of CNTs/S, it also possesses a uniform 3D-interwined structure in Figure 2(g). As shown in Figure 2(h and i), it can be observed that the

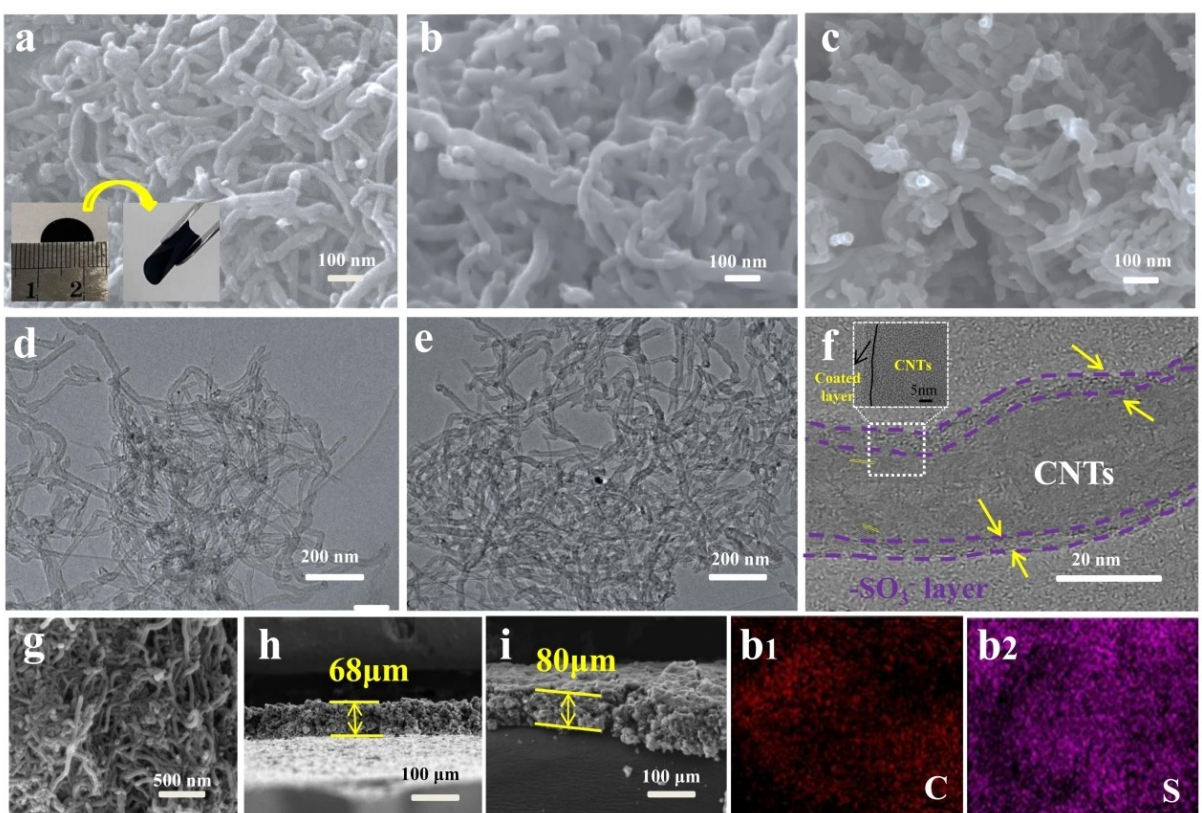


Figure 2. SEM images of a) self-supporting CNTs substrate, b) CNTs/S composite and c) M/S/M- SO_3Li . TEM images of d) self-supporting CNTs substrate, e) CNTs/S composite, and f) CNTs- SO_3Li . SEM profiles of g, h) CNTs/S, and i) M/S/M- SO_3Li . Mapping images of CNTs/S composite (b1) C, and (b2) S.

thickness of CNTs/S and M/S/M-SO₃Li electrodes are approximately 68 and 80 μm (CNTs-SO₃Li loading 2 mg).

2.2. Electrochemical Performance of Li-S Batteries

The areal loading mass of SO₃ groups is considered a vital factor for the electrochemical performance and cycling stability of Li-S batteries. Elemental analysis was conducted to quantify the content of SO₃ in CNT-SO₃Li (Table S2). To explore the optimal amount, CV and EIS were performed, as displayed in Figures 3(a and b). Compared with those with a content of 1 or 3 mg cm⁻² (based on the CNT-SO₃Li content), the CV plots of 2 mg cm⁻² present more intensive and sharper redox peaks and a smaller difference in the potential separation between the cathodic and anodic peaks, suggesting lower polarization and fast redox kinetics. Obviously, the M/S/M-SO₃Li electrode with 2 mg cm⁻² exhibits reduced internal and charge transfer resistance. Therefore, it is noteworthy that the content of the SO₃ groups is inversely related to the electronic and ionic conductivity and structural stability. The Li-S cells with different contents of SO₃ groups were measured at 0.2 C (Figure 3c). Benefiting from the fast electronic and ionic transport and the effective confinement of polysulfides, the M/S/M-SO₃Li electrode with 2.0 mg cm⁻² exhibits outstanding discharge specific capacities and cycling stability compared with the 1.0 and 3.0 mg cm⁻² loading masses, respectively.

The Li-S cell of the M/S/M-SO₃Li electrode with 2.0 mg cm⁻² delivers the highest initial discharge capacity of 1496.1 mAh g⁻¹ and still retains a discharge capacity of 1012.4 mAh g⁻¹ after 100 cycles, corresponding to a capacity retention of 68.05% and a Coulombic efficiency of $\geq 99\%$. By contrast, the cycling stability with high and low loading masses exhibits initial discharge capacities of 1128.7 and 1196.5 mAh g⁻¹, which gradually decrease to 613.1 and 721.8 mAh g⁻¹ with capacity retentions of 54.32% and 60.32%, respectively. Based on electrochemical test and BET results (Figure 1f), when decreased until a certain value, the SO₃ groups did not exert a function for the suppression of the shuttle effect via a binary electrocatalyst effect. By contrast, when largely increased, the reduced porosity will be adverse to electrolyte permeability, thereby resulting in sluggish electron and ion transfer and increased resistance. According to the above results, the

following electrochemical tests were conducted under 2 mg cm⁻².

The galvanostatic charge/discharge profiles of the M/S/M and M/S/M-SO₃Li electrodes were measured at 0.2 C, as shown in Figure 4(a). The profiles exhibit two typical discharge plateaus and two charge plateaus. The Li-S cell with the M/S/M-SO₃Li electrode clearly shows a lower voltage hysteresis of 162 mV compared to that of the M/S/M electrode with 192 mV, which verifies the decrease in polarization for the M/S/M-SO₃Li electrode.^[56] The enlarged charge/discharge profiles at 0.2 C were applied to evaluate the overpotential of interphase transformation kinetics between liquid polysulfides and solid Li₂S₂/Li₂S, as shown in the inset of Figure 4(a). In the initial region of the charge process, the M/S/M-SO₃Li electrode exhibits a relatively flat voltage valley, corresponding to a lower overpotential (45.6 mV) than that of the M/S/M electrode (102.6 mV). This suggests a lower delithiation and decomposition energy barrier for Li₂S,^[57] which may be because the SO₃ groups could efficiently weaken the Li-S bonds. Furthermore, the M/S/M-SO₃Li electrode also displays a lower voltage jump (26 mV) compared with that of the M/S/M electrode (39 mV) in the second plateau of the discharge process, implying a reduced overpotential and nucleation energy barrier from soluble Li₂S₆ to Li₂S.^[58] All the above results indicate the enhanced catalytic conversion ability of LiPS and decreased reaction barrier owing to the assistance of the SO₃ groups.

The cycling performance of the cell with the M/S/M-SO₃Li electrode exhibits higher discharge capacities than that of the M/S/M electrode at 0.2 C, as displayed in Figure 4(b). The Li-S cell assembled with the M/S/M-SO₃Li electrode exhibits a high initial discharge capacity of 1496.1 mAh g⁻¹, which eventually maintains 1012.4 mAh g⁻¹ after 100 cycles, corresponding to a capacity retention of 67.67% and a Coulombic efficiency of almost 100%. By contrast, the Li-S cell with the M/S/M electrode delivers an initial discharge capacity of 1364.2 mAh g⁻¹, which dramatically decays to 789.2 mAh g⁻¹ after 100 cycles, with a capacity retention of 57.85% and a Coulombic efficiency of 100%. To further understand the function of lithiated SO₃ groups in dominating the electrochemical performance, the low and high plateau capacities (denoted as Q_H and Q_L) were extracted from the charge/discharge curves at 0.2 C. For discharge, the Q_H and Q_L are related to soluble LiPS formation and Li₂S₂/Li₂S precipitation.^[59] As displayed in Figure 4(c), it can be seen that there are

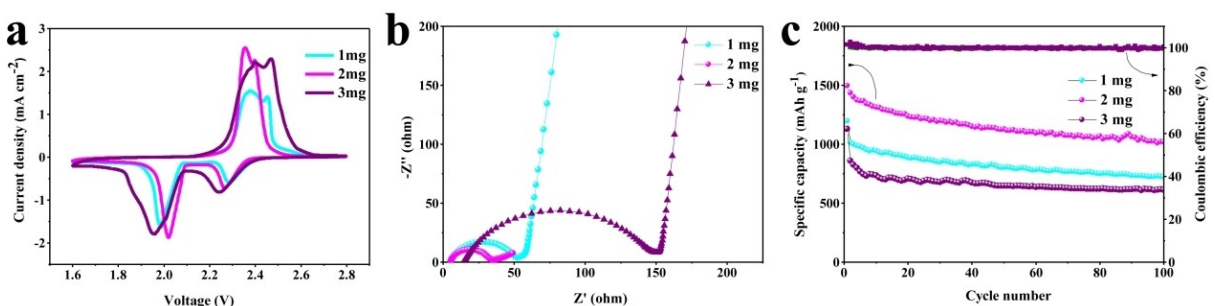


Figure 3. M/S/M-SO₃Li electrode with different sulfonated loadings: a) CV curves, b) EIS spectra, and c) cyclic performance at 0.2 C.

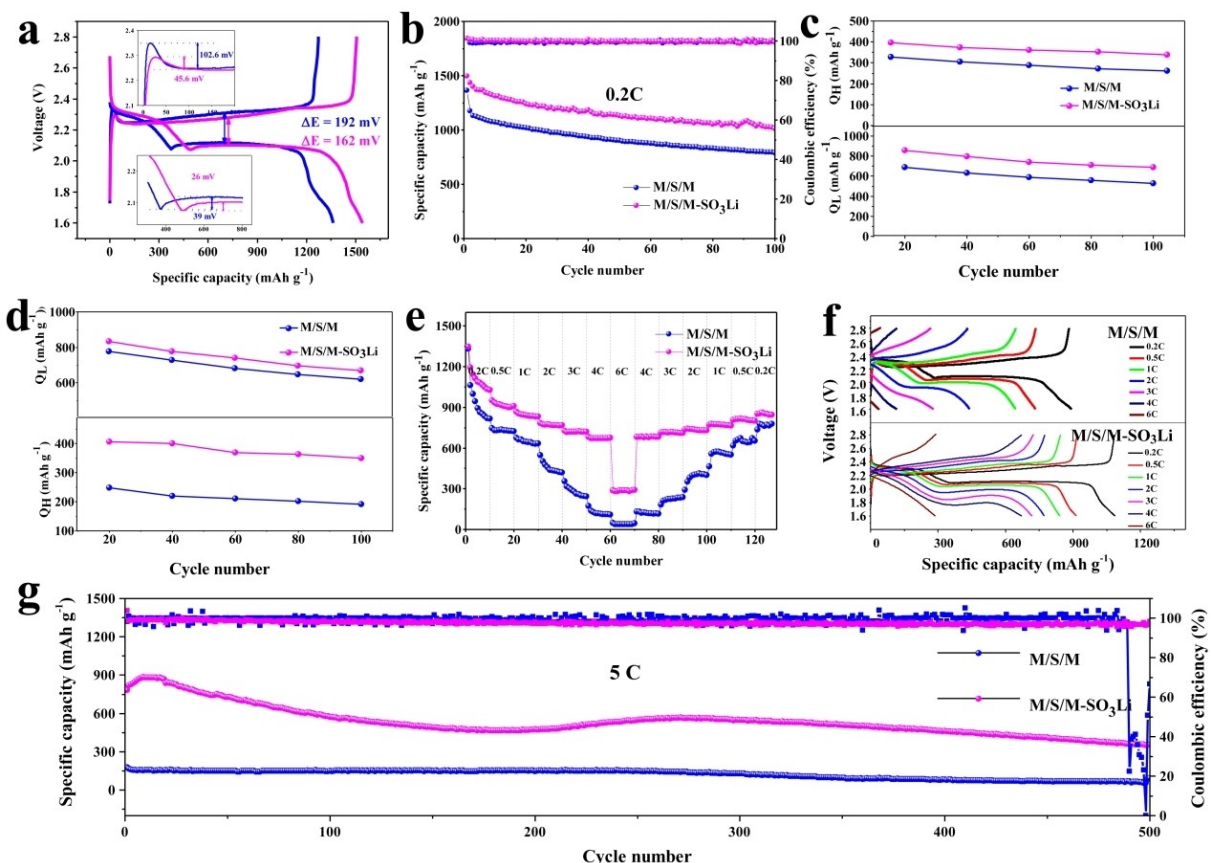


Figure 4. a) Galvanostatic charge-discharge profiles of M/S/M and M/S/M-SO₃Li electrodes at 0.2 C of initial cycle. b) Cyclic performance of M/S/M and M/S/M-SO₃Li electrodes at different cycle: c) discharge plateau, and d) charge plateau. e) Rate performance from 0.2 C to 6 C. f) Charge/discharge profiles of M/S/M and M/S/M-SO₃Li electrodes at different current densities. g) Long-term cycling performance of M/S/M and M/S/M-SO₃Li electrodes at 5 C.

apparent differences from the values of Q_H and Q_L . Noticeably, the M/S/M-SO₃Li electrode displays higher Q_H and Q_L values and plateau capacity retention compared with those of the M/S/M electrode, resulting in accelerated LiPS conversion kinetics and the uniform precipitation of Li₂S₂/Li₂S. For charging, Q_L and Q_H are associated with the decomposition of Li₂S to LiPS and S₈ formation, depicted in Figure 4(d). For comparison, the M/S/M-SO₃Li electrode with higher Q_H and Q_L indicates that the lithiated SO₃ layer promotes the decomposition and transformation of Li₂S and the conversion of LiPS to S₈.

Figure 4(e) shows the cell based on the M/S/M-SO₃Li electrode with excellent capacity performance. When the M/S/M-SO₃Li electrode is cycled at rates of 0.2, 0.5, 1, 2, 3, 4 and 6 C, it delivers impressive discharge capacities of 1088.1, 914.3, 841.9, 771.5, 719.3, 671.5 and 288.5 mAh g⁻¹, respectively. When switched back to 4, 3, 2, 1, 0.5 and 0.2 C, the discharge specific capacities are 684.2, 718.3, 735.4, 773, 814.3 and 849.7 mAh g⁻¹ respectively. By contrast, the Li-S cell with the M/S/M modified electrode delivers far inferior discharge capacities of 894.3, 734.5, 645.8, 439.6, 279.3, 117.6 and 38.5 mAh g⁻¹ at various rates, respectively, and almost has no capacity at 4 and 6 C. When the current density returns, it provides capacities of 122.2, 225.3, 402.2, 571.6, 651.1 and 770.9 mAh g⁻¹, respectively. Comparing the voltage profiles of

the M/S/M and M/S/M-SO₃Li electrodes in Figure 4(f), the M/S/M-SO₃Li electrode obviously displays a slighter voltage hysteresis and longer plateau region with progressive current rates from 0.2 to 6 C, indicating the rapid redox reaction kinetics and the low overpotential of Li₂S deposition. In addition, the cell with the M/S/M-SO₃Li electrode always holds higher Q_H and Q_L and lower polarization at different current densities (Figures S2a and b).

Figure 4(g) exhibits the long-term cycling stability of the M/S/M and M/S/M-SO₃Li electrodes at a high current density of 5 C. Notably, the M/S/M-SO₃Li electrode delivers a relatively low initial discharge capacity of 783.5 mAh g⁻¹, relating to the inadequate activation, and thereby undergoes the rearrangement of the sulfur component, along with low capacity fading of only 0.1% per cycle. In comparison, the discharge capacity of the M/S/M electrode only reaches 91 mAh g⁻¹ after 500 cycles.

2.3. Kinetic Analysis of Li-S Batteries with M/S/M-SO₃Li

To obtain insight into the electrochemical behavior of the M/S/M-SO₃Li electrode for the rapid redox reaction of LiPS, the EIS measurements are depicted in Figure 5(a). It can be seen that the Nyquist plots for the M/S/M and M/S/M-SO₃Li electrodes

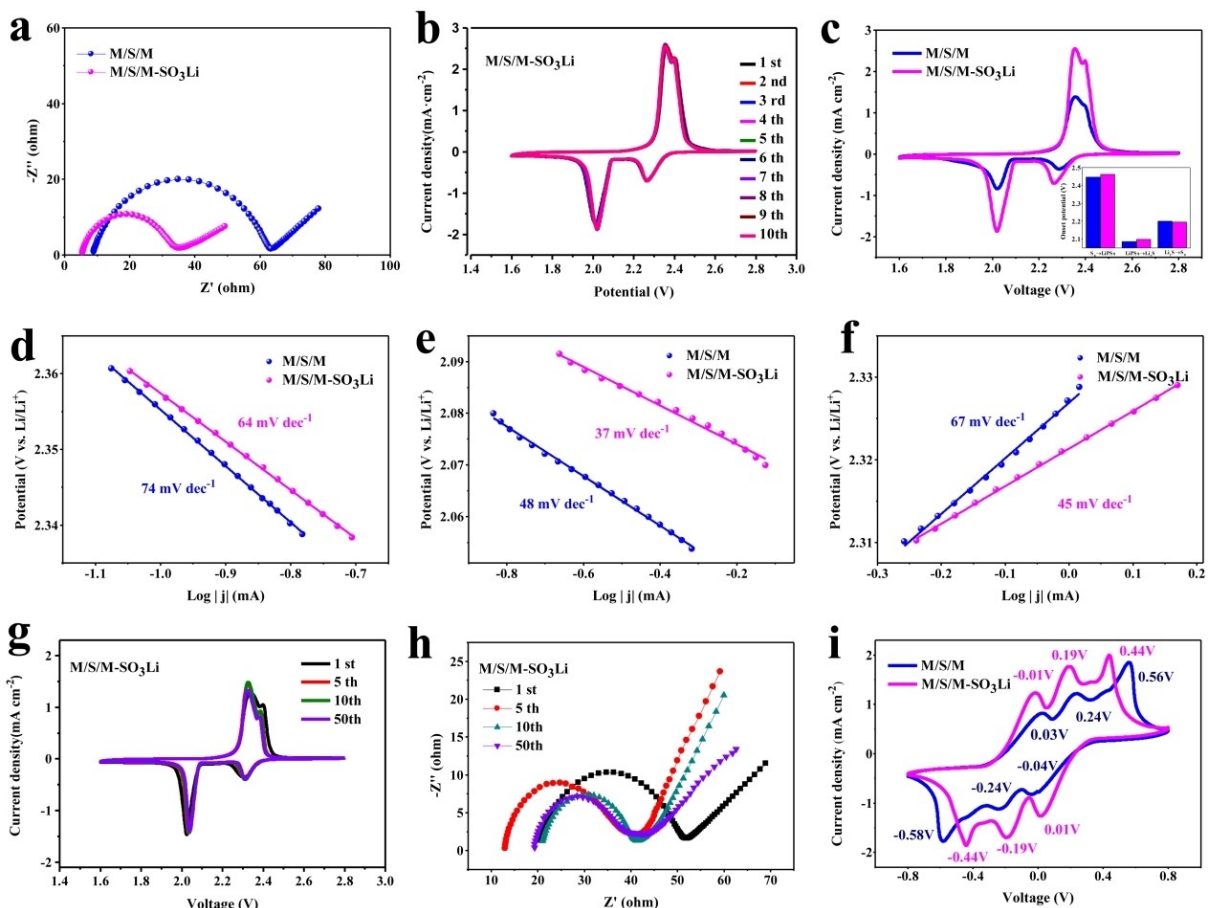


Figure 5. a) EIS spectra of M/S/M and M/S/M-SO₃Li electrodes. b) CV curves of M/S/M-SO₃Li electrode at 0.1 mV s⁻¹. c) CV curves of M/S/M and M/S/M-SO₃Li electrodes with the insert of onset potential at 0.1 mV s⁻¹. Tafel plots with M/S/M and M/S/M-SO₃Li electrodes d) at cathodic process ($S_8 \rightarrow Li_2S_x$ ($4 \leq x \leq 8$)), e) at cathodic process (Li_2S_x ($4 \leq x \leq 8$) $\rightarrow Li_2S_2/Li_2S$), and f) at anodic process. M/S/M-SO₃Li electrode after 1, 5, 10 and 50 cycles: g) CV curve and h) EIS spectra. i) CV curves of symmetric cells with different electrodes at 0.5 mV s⁻¹.

are composed of a semicircle in the high-frequency region, corresponding to charge transfer resistance (R_{ct}), and one sloping line in the low-frequency region associated with the Li⁺ diffusion process (W_o).^[60] The EIS curve of the M/S/M-SO₃Li electrode delivers a much smaller charge transfer resistance (28 Ω) than that of the M/S/M electrode (54 Ω), demonstrating a faster charge transfer at the electrode/electrolyte interface and enhanced redox kinetics for LiPS transformation, which is consistent with the excellent electrochemical performance of the M/S/M-SO₃Li electrode.

In order to further investigate the effect of lithiated SO₃ groups on the electrochemical features, the typical CV profiles of the M/S/M-SO₃Li and M/S/M electrodes are presented in Figure 5(b and c). In the subsequent ten cycles, the CV curves of the M/S/M-SO₃Li electrode in Figure 5(b) remain almost constant with respect to the current and voltage of all peaks, indicating the excellent electrochemical reversibility and stability of the dynamic process. For comparison, the M/S/M-SO₃Li electrode exhibits sharper peaks and a stronger current magnitude, suggesting rapid redox kinetics from the electrochemical reaction (Figure 5c). Accordingly, it is noted that the onset potential for the M/S/M-SO₃Li electrode exhibits a

distinguishable positive shift in the reduction process and a negative shift in the oxidation process compared with those of the M/S/M electrode, as shown in the inset of the CV curves. This reflects the considerably smaller polarization and superior electrocatalytic activity, in good agreement with the observations from the galvanostatic charge/discharge measurements (Figure 4a). The potential shift is assigned to the presence of lithiated SO₃ groups, which is further verified by the Tafel slopes based on the corresponding CV curves.

As displayed in Figures 5d-f, the M/S/M-SO₃Li electrode always shows lower Tafel slopes (37 and 64 mV dec⁻¹ for the cathodic peaks and 45 mV dec⁻¹ for the anodic peak) than those of the M/S/M electrode (48 and 74 mV dec⁻¹ for the cathodic peaks and 67 mV dec⁻¹ for the anodic peak). This demonstrates the enhanced electrocatalytic conversion of LiPS to solid Li₂S_x/Li₂S in the M/S/M-SO₃Li electrode.^[61] Thus, the presence of lithiated SO₃ groups not only facilitates the rapid transport of Li⁺ and electrons but also accelerates the rapid redox kinetics by means of suppressing the polysulfide diffusion and reversible transformation.

To some extent, the smaller the current density, the longer the charge/discharge time, so the dissolution of polysulfides

becomes more serious. Thus, the cycling stability at low current density can be employed to assess the polysulfide shuttle behaviors. Figure 5(g) shows the CV curves of the M/S/M-SO₃Li electrode after 1, 5, 10 and 50 cycles at 0.2 C. Remarkably, no obvious variation or unfading peak current in all the CV profiles were observed. This confirms the efficiently suppressed LiPS diffusion and dynamic equilibrium of the sulfur component during the charge/discharge process, which essentially originate from the reduced overpotential of Li₂S nucleation and accelerated reversible conversion of Li₂S to Li₂S₂. This is further certified by the basically unchanged charge/discharge plateaus at various cycles (Figure S3).

To ascertain the positive effect of the lithiated SO₃ groups for Li₂S species, EIS spectra was conducted during the M/S/M-SO₃Li electrode cycling, as shown in Figure 5(e). It is widely acknowledged that the charge transfer resistance increases due to the deposition and insulation of Li₂S, leading to sluggish redox kinetics. However, the charge transfer resistance of the M/S/M-SO₃Li electrode gradually decreases with cycling, implying that it not only propels the LiPS electrocatalytic conversion but also reduces the irreversible loss of sulfur species by facilitating the electrochemical reversibility of Li₂S, in agreement with the results in Figures 5(d-f). In addition, it is noteworthy that all the Nyquist plots are only composed of one semicircle even after cycling. When two semicircles exist, they are related to the SEI film caused by solid Li₂S₂ and Li₂S at high frequency^[62] and charge transfer resistance at medium frequency, respectively, demonstrating the promoted decomposition of Li₂S.

To gain better insight into the catalytic conversion kinetics of the LiPS, the CV curves of symmetric cells with a 0.2 M Li₂S₆ electrolyte were measured with two identical electrodes from -0.8 to 0.8 V, as presented in Figure 5(i). The curve of the

M/S/M-SO₃Li electrode displays three pairs of highly reversible redox peaks at -0.01/0.01 V (reduction of S to Li₂S₆ and oxidation of Li₂S to Li₂S₂), -0.19/0.19 V (reduction of Li₂S₆ to Li₂S₂ and oxidation of Li₂S₂ to S) and -0.44/0.44 V (reduction of Li₂S₂ to Li₂S and oxidation of Li₂S₂ to Li₂S)^[63,64] For the M/S/M electrode, these peaks appear at -0.04/0.03, -0.24/0.24 and -0.58/0.56 V, thereby confirming the considerable improvement in the electrode stability and the immobilization and utilization of sulfur species. Moreover, the M/S/M-SO₃Li electrode exhibits a significantly higher peak current, sharper peaks and smaller polarization than that of the M/S/M electrode. This demonstrates that the lithiated SO₃ groups are favorable for propelling the LiPS conversion to uniform nucleation in the discharge process and the decomposition of Li₂S in the charge process.

2.4. Calculation of Li⁺ Diffusion Coefficient

To understand the reason for the superior electrochemical performance of the cells with the M/S/M-SO₃Li electrode, the Li⁺ diffusion coefficient (D_{Li}^{+}) was calculated based on the corresponding CV curves at different scanning rates (Figure S4), as presented in Figures 6(a-c). It is noted that the increased peak current displays a good linear correlation with the square root of the correspondent scanning rate, confirming that this dynamic reaction is the diffusion-controlling step, where D_{Li}^{+} can be evaluated, guided by the Randles-Sevcik equation.^[65] According to the positive correlation between I_p and $v^{1/2}$, the steeper the slope, the larger the D_{Li}^{+} . Notably, the M/S/M-SO₃Li electrode always possesses higher slopes with respect to the M/S/M electrode during the charge/discharge process, indicating that the lithiated SO₃ component is beneficial for fast Li⁺

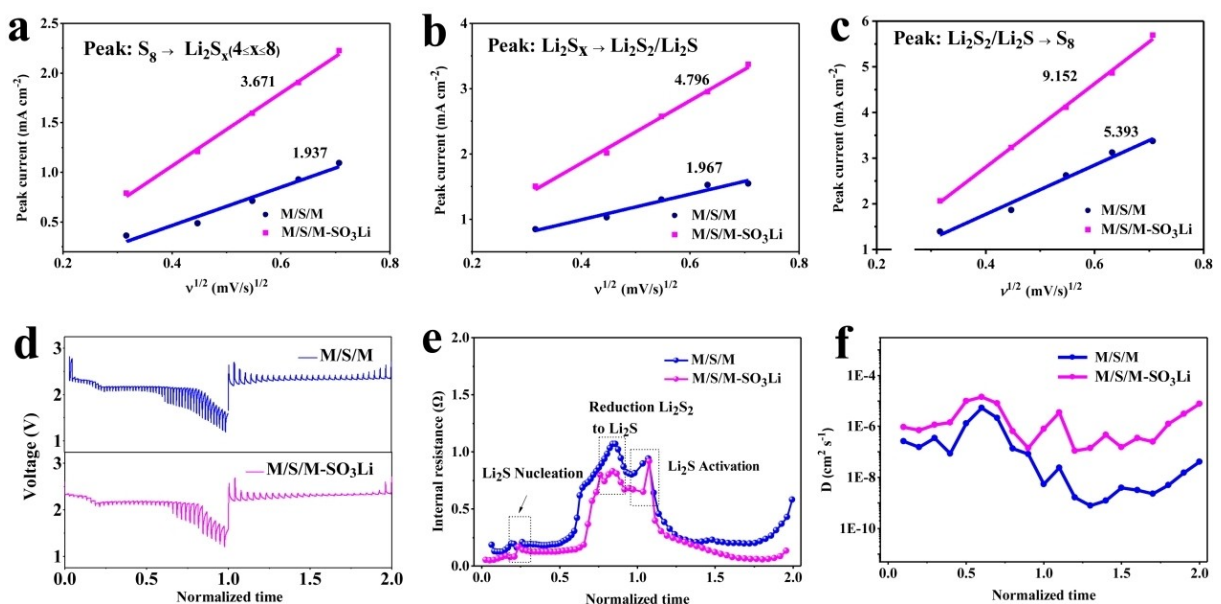


Figure 6. The plots of peak current (I_p) versus the square root of the scan rate ($v^{1/2}$): a) at reduction peak of 2.3 V, b) at 2.1 V, and c) at oxidation peak of 2.4 V. d) GITT curves of M/S/M and M/S/M-SO₃Li electrodes during the charge-discharge process. e) The calculated internal resistance based on GITT. f) The calculated Li⁺ diffusion coefficients from GITT curves.

diffusion. It is well known that LiPS dissolved in the electrolyte may react with the Li anode and consume a certain amount of electrolyte, leading to higher electrolyte viscosity, thereby decreasing the transfer rate of Li^+ during the redox reaction. Therefore, these observations reveal that the lithiated SO_3 groups can considerably impede the shuttle effect of LiPS and improve their redox kinetics. More importantly, rapid Li^+ diffusion with the M/S/M- SO_3Li electrode can guarantee significant Li^+ concentrations for polysulfide conversion, thereby reducing the consumption of the Li anode and then slowing down the anode corrosion and Li dendrite growth.

The galvanostatic intermittent titration technique (GITT) was employed to perform real-time monitoring for the reversible conversion of Li_2S_n during the electrochemical process. From Figure 6(e), it can be observed that the M/S/M- SO_3Li electrode exhibits a smaller internal resistance and higher D_{Li^+} in comparison with the M/S/M electrode, which can be evaluated according to detailed calculation formula (Supporting Information) by the GITT potential profiles (Figure 6d).^[66,67] Based on the reaction mechanism in Li-S batteries, the

conversion of Li_2S_2 to Li_2S presents the largest positive Gibbs energy barrier of all the steps, so this solid-solid transformation is considered the rate-limiting step,^[68] in agreement with the largest internal resistance and decreased D_{Li^+} (Figure 6f) in the whole charge/discharge process. Hence, these observations demonstrate that the lithiated SO_3 groups not only boost the electrocatalytic conversion from Li_2S_6 to $\text{Li}_2\text{S}/\text{Li}_2\text{S}$ but also reduce the nucleation and growth energy barriers from LiPS to Li_2S ($\text{LiPS} \rightarrow \text{Li}_2\text{S}_2 \rightarrow \text{Li}_2\text{S}$) and decrease the Li_2S decomposition barrier for the charge procedure.

2.5. Inhibition of Polysulfides Shutting of Li-S Batteries

To further elucidate the interactions between lithiated SO_3 groups and LiPS for the nucleation and deposition of Li_2S , SEM was carried out for the different electrodes and Li anodes after cycling, as presented in Figures 7(a-d). As shown in Figure 7(a), it can be clearly observed that the surface of the M/S/M electrode forms a large aggregate and almost blocks the entire

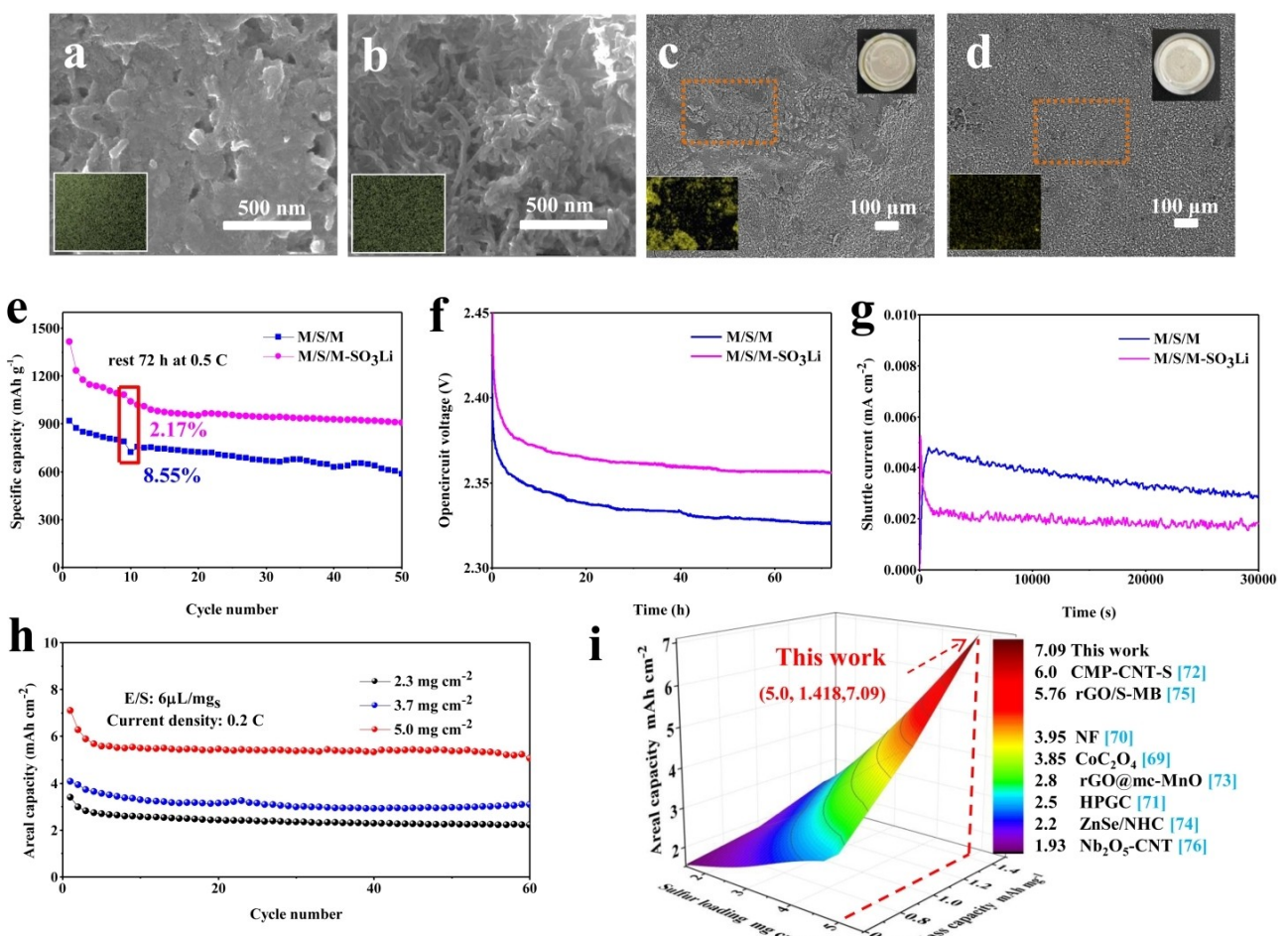


Figure 7. SEM images of the disassembled cells after 100 cycles at 0.2 C: a) M/S/M electrode surface, and b) M/S/M- SO_3Li electrode surface. Digital and SEM images of Li anode surface with S element mapping from c) cell assembled with M/S/M, and d) cell assembled with M/S/M- SO_3Li electrode. e) Self-discharge behavior of M/S/M and M/S/M- SO_3Li electrodes. f) OCV profiles of M/S/M and M/S/M- SO_3Li electrodes during rest time. g) Shuttle current measurement of M/S/M and M/S/M- SO_3Li electrodes. h) Cycling performance of Li-S batteries with the M/S/M- SO_3Li electrode at high sulfur loading and lean electrolyte. i) Comparison of this work and recent literature.

channel structure. This is associated with significant LiPS decoupling from the sulfur matrix and dissolution in the electrolyte to eventually form “dead sulfur” that deposits on the electrode surface, leading to the sluggish electrochemical reactions. In comparison, the M/S/M-SO₃Li electrode shown in Figure 7(b) maintains the original 3D interconnected network with the developed residual pore structure and adsorbs a significant amount of uniform sulfur species, implying a clear shielding effect for the LiPS shuttle behaviors and ensuring fast charge transfer and Li⁺ transport. SEM for the cycled Li anode was applied to provide deeper insight into how to impact the formation of Li₂S.

As can be seen from Figure 7(d), the Li anode with the M/S/M-SO₃Li electrode is relatively smooth without apparent corrosion and degradation. In contrast the M/S/M electrode (Figure 7c) is very rough with flake-like and agglomerate solid particles, resulting in destruction of the integrity of the SEI film along with increased internal impedance and aggravation of the growth of lithium dendrites. This result suggests that cycled Li tends to rearrange toward homogeneous deposition with the aid of the M/S/M-SO₃Li electrode. Based on the observations from mapping, the S element on the Li anode accompanied with the M/S/M-SO₃Li electrode is much weaker and more homogeneously distributed in comparison with the M/S/M electrode. This reveals that the existence of lithiated SO₃ groups can effectively suppress the LiPS migration toward the anode side and promote the uniform deposition of Li₂S with reduced overpotential and faster Li⁺ transport than the reaction consumption, thereby accelerating the solid phase transformation kinetics.

The self-discharge phenomenon is regarded as another important indicator for evaluating the inhibitory effect for polysulfide diffusion. As displayed in Figure 7(e), the cycling performance at 0.5 C with the M/S/M-SO₃Li electrode, along with a 72 h rest time after the ninth cycle, shows a 2.17% self-discharge ratio, which is in sharp contrast to the M/S/M electrode with 8.55% (Figure S5). In addition, Figure 7(f) shows the variation in the open-circuit voltage (OCV) profiles during the rest time. In contrast, a more obvious OCV drop can be found for the M/S/M electrode, which is indicative of inferior retardation of LiPS compared with the M/S/M-SO₃Li electrode due to extensive LiPS passing through the electrode toward the anode.

The suppression of LiPS diffusion is the prerequisite for prominent electrochemical performance along with improved cycling stability and high sulfur diffusion utilization. To verify our hypothesis regarding the capability of the M/S/M-SO₃Li electrode toward the blocking LiPS shuttle effect, the shuttle current measurement was performed as charged to 2.38 V^[68] as shown in Figure 7(g). As time proceeds, the shuttle current of the M/S/M-SO₃Li electrode is obviously lower than that of the M/S/M electrode, demonstrating the absence of lithiated SO₃ groups on the substrate surface, which inhibits the overflow from the electrode into electrolyte. This result is also further evidenced by the SEM characterization after electrode and Li anode cycling.

To further validate the superiority of the M/S/M-SO₃Li electrode for more practical applications, it was used with a high sulfur loading of 2.3–5.0 mg cm⁻², even for a 6 μL mg s⁻¹ lean electrolyte. As displayed in Figure 7h, the M/S/M-SO₃Li electrode with a sulfur loading of 2.3 mg cm⁻² obtains an initial areal capacity of 3.4 mAh cm⁻² and still retains 2.21 mAh cm⁻² after 60 cycles at 0.2 C. When the sulfur mass loading is further increased to 3.7 and 5.0 mg cm⁻², the reversible areal capacity reaches 4.08 and 7.09 mAh cm⁻² and maintains 3.09 and 5.07 mAh cm⁻² after 60 cycles, respectively. In addition, the M/S/M-SO₃Li electrode still exhibits an obvious charge/discharge plateau with relatively low polarization and satisfactory cycling stability, illustrating its potential for future Li–S batteries due to its fast electron and ion strong LiPS shielding and rapid polysulfide conversion kinetics. Furthermore, to better compare the effect of the electrolyte on the electrode, we decrease it from 15 to 6 μL mg s⁻¹ with the same sulfur loading and observe that the discharge specific capacity changed at a comparatively low level, indicating its potential for practical applications in the case of lean electrolyte (Figure S6). By comparing with other works, the superiority of the M/S/M-SO₃Li electrode is further highlighted in Figure 7(i).^[69–76]

To further clarify the possible chemical interactions between sulfur species and M/S/M-SO₃Li electrode at atomic level, DFT theoretical calculations were carried out to evaluate the adsorption energy and structure stability. Guided by the results in Figure 8, the adsorption energy between SO₃⁻ groups and Li₂S (2.38 eV) and Li₂S₆ (1.72 eV) were more positive than that of NH₄⁺ in DC5700, corresponding values of Li₂S (1.95 eV) and Li₂S₆ (0.55 eV), which are not enough to induce the cleavage and formation of Li–S chemical bonds, reasonably indicating the SO₃⁻ groups on M/S/M-SO₃Li electrode exert a paramount adsorption effect toward sulfur species and mitigate LiPS dissolution and shuttle effect, nor NH₄⁺ group. The result agrees with the electrochemical data of M/S/M-SO₃Li and M/S/M-NH₄⁺ in Figures S7 and S8. In addition, it can be observed that when putting Li₂S and Li₂S₆ on the side of SO₃⁻ group, the Li–S bond length is longer than existing apart (in Figure S9), which implies the positive effect of SO₃⁻ groups can effectively weaken the Li–S bond via forming of Li–O bond, which is beneficial to reduce the decomposition energy barrier of LiPS and Li₂S.

To further reveal the nature of the host-guest interaction, XPS measurements of the fully charged M/S/M-SO₃Li electrode after 100 cycles were performed. As shown in Figure 9(a), the S2p XPS spectra can be differentiated into six subpeaks, where the two centered at 162.5 and 164.1 eV correspond to the terminal (S_T⁻¹) and bridging sulfur (S_B⁰) due to strong chemisorption, respectively.^[77] The S2p peaks located at 168.8 and 167.2 eV are attributed to the formation of thiosulfates and polythionates, respectively, originating from the catalytic effect of the lithiated SO₃ groups propelling the conversion of LiPS. This corroborates the strong bonding interaction between the SO₃ electrocatalyst and LiPS. The characteristic peak of S–O at 170.0 eV slightly shifts toward a higher binding energy by 0.1 eV in comparison with that of CNT-SO₃Li, implying the existence of significant Li⁺ concentrations around the

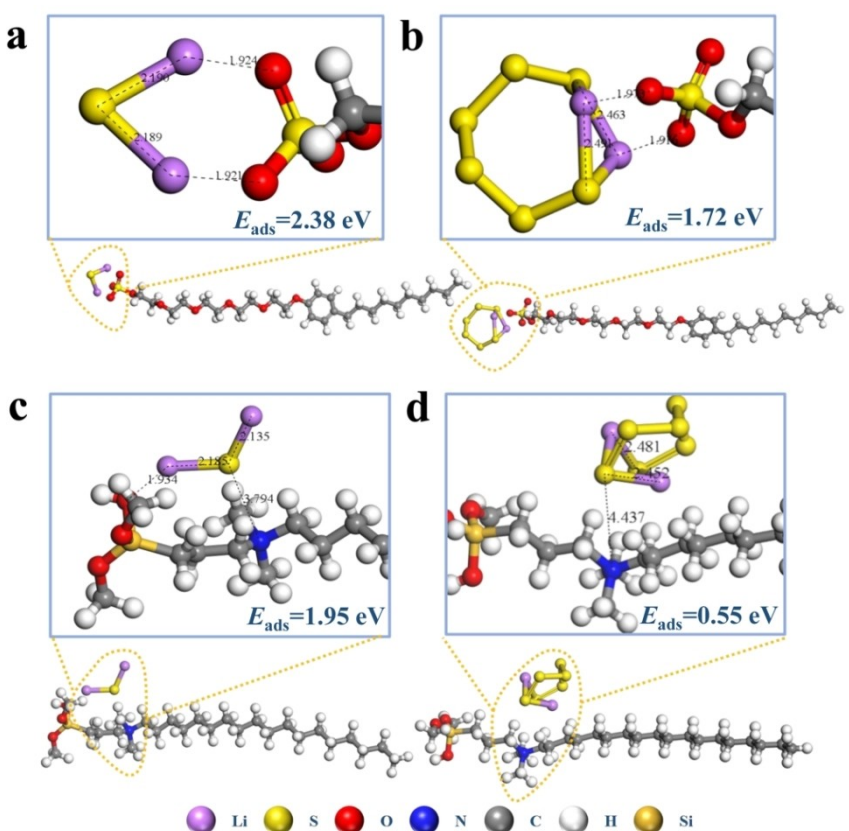


Figure 8. The correspond adsorption energy and bond length on substrate I with NPES a) for Li_2S , and b) for Li_2S_6 . Substrate II with DC5700 c) for Li_2S , d) for Li_2S_6 .

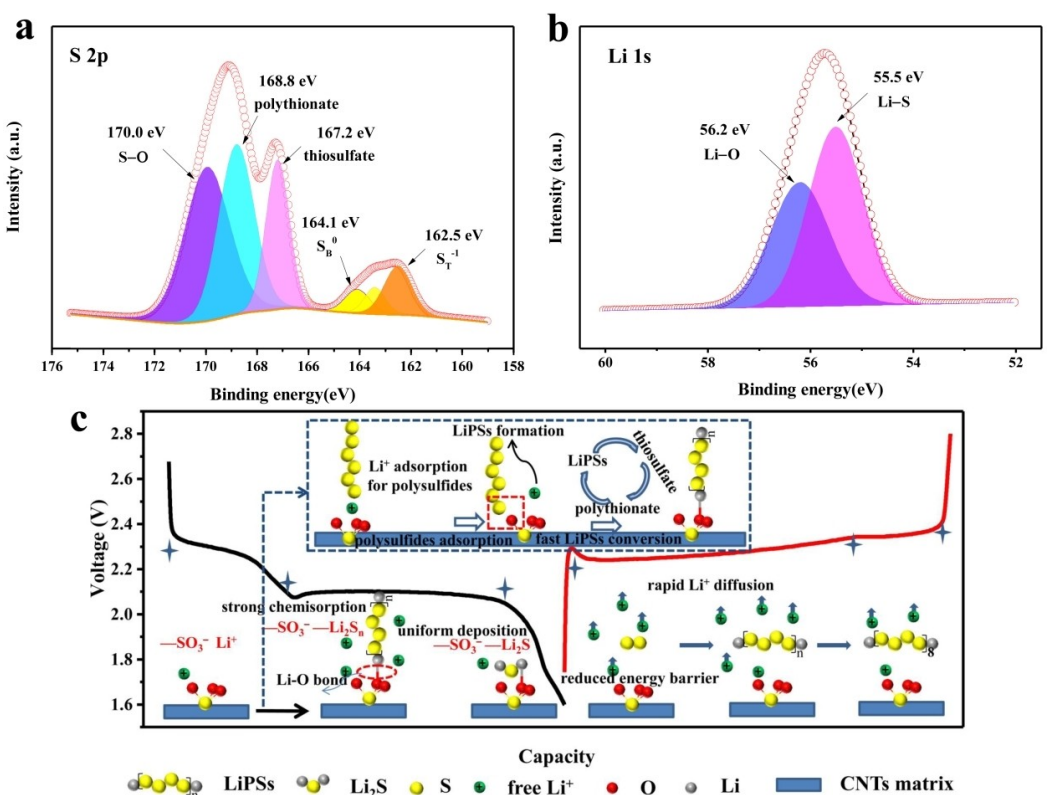


Figure 9. XPS spectra of M/S/M- SO_3Li electrode after 100 cycles: a) S 2p, and b) Li 1s. c) Mechanism schematic of M/S/M- SO_3Li electrode during cycling.

$\text{LiSO}_3\text{-Li}_2\text{S}_x$ complex. As further certified by the Li 1s spectrum in Figure 9b, the emergence of Li–O at 56.2 eV, where O is from SO_3 groups and Li is from LiPS and not LiTFSI due to the more stable chemical bonds between SO_3 and LiPS,^[17,78] thereby confirming the interaction between LiPSs and the catalyst host, consistent with the DFT results.

To better understand the binary electrocatalytic role of SO_3 groups, we propose a reasonable catalytic reaction mechanism based on the above results shown in Figure 9(c). During discharge, there are two different pathways that involve the conversion of LiPS via a dual synergistic interaction. One is to boost the reversible conversion of LiPS to Li_2S through the formation of a thiosulfate-polythionate transfer mediator, accompanied by significant amounts of Li^+ surrounding the catalytic active sites, thereby ensuring the homogeneous nucleation and deposition of insoluble $\text{Li}_2\text{S}/\text{Li}_2\text{S}_2$. The other pathway is to capture and further catalyze LiPS on the catalyst surface via the Li–O bond interaction between the LiPS and SO_3^- groups. In more detail, the polysulfides dissolved in the electrolyte were adsorbed via a Li^+ electrostatic effect, as a result of the interaction between Li^+ and SO_3^- by ionic and covalent bonds. This reveals that Li^+ ions tend to react with polysulfides to produce LiPS, accompanied by electron transfer from SO_3^- to LiPS, resulting in accelerated LiPS conversion.

Furthermore, due to the interaction between SO_3^- and LiPSs, the produced thiosulfates and polythionates promote the electrocatalytic transformation of LiPS. When charging, Li^+ ions have a tendency to fast diffuse toward the Li anode driven by the electric field and concentration gradient. According to the principle of charge balance and Lewis acid-base theory, the negative SO_3^- tends to obtain Li^+ from the solid Li_2S . Owing to Li–O having a higher binding energy than Li–S (Figure 9b), it is further verified that Li^+ can bind with SO_3^- in a facile manner. Thus, the translation of Li_2S into polysulfides results in a lower decomposition energy barrier of Li_2S and a rapid delithiation process. Moreover, the improved Li^+ diffusion behavior not only provides a guarantee for rapid reduction reaction kinetics but also ensures that the diffusion rate of Li^+ is larger than the reaction rate. This therefore degrades the reaction between the LiPS and Li metal and reduces the corrosion of the Li anode and the growth of Li dendrites due to the shuttle effect.

3. Conclusions

In summary, we have rationally designed a 3D flexible multifunctional M/S/M- SO_3Li electrode as an effective host for high-performance Li–S batteries. Benefiting from structural synergistic effect, the cells assembled with M/S/M- SO_3Li electrode exhibits significantly depressed shuttle effect, the high utilization of sulfur species and Li anode protection, in which, CNTs substrate with 3D porous skeleton

can provide continuously long-range conductive network and physical restriction, ensuring fast electronic transfer and ion diffusion. Besides, CNTs substrate plays the key roles for regulating the deposition of Li_2S with 3D porous channels, thus promoting electrochemical redox kinetics during charge and

discharge process. On the other hand, the lithiated SO_3 groups not only provide strong chemisorption, electrostatic force and catalytic activity sites for LiPS, and thus effectively suppress the shuttle behavior and accelerate the conversion kinetics between LiPS and Li_2S . Meanwhile, the SO_3 groups also promote the uniform nucleation of Li_2S and decreased Li_2S decomposition barrier, thus achieving the high utilization of sulfur and inhibiting the growth of irregular Li dendrite. Based on the synergy of above advantages, the cell with M/S/M- SO_3Li electrode displays excellent cycle stability (even at 5.0 mg cm^{-2} high sulfur loading vs. 1.5 mg cm^{-2}), ultra-long lifespan, superior rate capability (783.5 mAh g^{-1} at 5 C vs. 91 mAh g^{-1}) and high sulfur loading (5.0 mg cm^{-2} vs. 1.5 mg cm^{-2}), low anti-self-discharge behavior (2.17% vs. 8.55%), admirable specific capacity (1012.4 mAh g^{-1} after 100th at 0.2 C vs. 789.2 mAh g^{-1}), compared with the M/S/M electrode, which provides a new strategy toward advanced Li–S batteries.

In short, although our M/S/M- SO_3Li electrode strategy can significantly suppress the LiPS shuttling and improve redox reaction kinetics, the dissolution of LiPS is inevitable from cathode to electrolyte. Thus, it is key to not only need to modify the sulfur cathode, but also need to decorate the membrane, electrolyte and Li anode.

Experimental Section

Preparation of free-standing CNTs substrate

The multi-walled carbon nanotubes (CNTs) were mixed with polyvinylidene fluoride (PVDF) binder at 8:1 ratio to form uniform slurry in N-methyl pyrrolidone (NMP) solution, which was coated onto Al foil current collectors and dried in an oven at 60 °C for 12 h. The CNT film was then peeled off from the Al foil and punched into small disks with a diameter of 12 mm, and the weight of 2.5–3.5 mg.

Preparation of CNTs/S composite

Sulfur powder was dispersed in an appropriate amount of carbon disulfide (CS_2) solution. Then, the solution was injected on the surface of CNTs film at 50 °C. The S/CNTs electrode heated in a glass bottle at 155 °C for 10 h.

Preparation of M/S/M- SO_3Li

The oxidized CNTs (CNTs-OH) reacted with DC5700 ($(\text{CH}_3\text{O})_3\text{Si}(\text{CH}_2)_3\text{N}^+(\text{CH}_3)_2(\text{C}_{18}\text{H}_{37})\text{Cl}^-$), and then with NPES ($\text{C}_9\text{H}_{19}\text{C}_6\text{H}_4\text{O}-(\text{CH}_2\text{CH}_2\text{O})_{10}\text{SO}_3^- \text{Na}^+$) to obtain CNTs- SO_3^- , which minutely described in previous works^[23]. Then the as-prepared CNTs- SO_3Li product was transferred into lithium hydroxide aqueous solution for thorough extraction of Na ions. After treated 24 h at room temperature, the CNTs- SO_3Li powder was separated by centrifugation, followed repeatedly washed with deionized water until neutral. After drying 60 °C for 12 h, the final product was collected. After that, absolute CNTs- SO_3Li powder was homogeneously dispersed into isopropanol solution by stirring and sonicating, and then coated to the CNTs/S electrode surface and dried at 60 °C. The M/S/M- SO_3Li electrode with different content of sulfonic groups was obtained by controlling the amount of coating. By comparison,

the M/S/M electrode was also prepared following the same procedure, with the difference of CNTs-SO₃Li and CNTs.

Materials characterization

The morphology and structure of the samples were characterized by using scanning electron microscopy (SEM, FEI Nova NanoSEM 430, 15 KV) and transmission electron microscopy (TEM, Fecnai F20, 200 KV). The X-ray diffraction (XRD) was conducted by a Rigaku diffractometer with Cu K α radiation at a scanning rate of 4° min⁻¹. Raman measurement was recorded on a Jobin Yvon Lab RAM HR800 instrument with a 532 nm Renishaw system. The Fourier transform-infrared spectroscopy (FT-IR) was measured by a TENSOR27. The X-ray photoelectron spectroscopy (XPS) was analyzed in Thermo scientific MVLTILAB2000 Base system with X-ray.

Electrochemical measurement

Coin cells (2025-type) were assembled in an argon-filled glovebox. The CNTs electrode was cut into circular disks with a diameter of 12 mm. Lithium metal foil and commercial PP separator were used as the anode and porous separator, respectively. The electrolyte was prepared by 1 M lithium bis(trifluoro-methanesulfonyl) imide (LiTFSI) dissolved in 1,3-dioxolane (DOL) and 1,2-dimethoxyethane (DME) with 0.2 M lithium nitrate (LiNO₃) as the additive. The typical sulfur loading was ~1.5 mg cm⁻² with E/S (electrolyte/sulfur) ratio of 15 μ L mg s⁻¹ in M/S/M and M/S/M-SO₃Li electrodes, while the high sulfur loading with 2.3–5.0 mg cm⁻² was 6 μ L mg s⁻¹ in M/S/M-SO₃Li electrode. The mass of sulfur in CNTs/S complex is also ~1.5 mg cm⁻². The galvanostatic charge-discharge electrochemical measurements were carried out using a LAND instrument in a voltage window of 1.6–2.8 V. The cyclic voltammetry (CV) and electrochemical impedance spectroscopy (EIS) measurement was conducted on multichannel electrochemical workstation. The CV was performed in a range between 1.6 and 2.8 V with a scan rate of 0.1 mV s⁻¹. The CV curves of symmetric cells were measured at a scan rate of 0.5 mV s⁻¹ in a voltage range of -0.8–0.8 V. EIS measurements of the coin cells were performed at open-circuit voltage over a frequency range of 0.01~10⁵ Hz with a sinusoidal voltage of the amplitude of 10 mV. The galvanostatic intermittent titration technique (GITT) was performed with a current pulse of 0.2 C for 5 min and rest for 0.5 h. The Li–S cells with LiNO₃-free were cycled one cycle at 0.2 C, and then discharged to 2.38 V and test the shuttle current under potentiostatic. All the electrochemical measurements were carried out at 25 °C.

Acknowledgements

We acknowledge the funding support from the Applied Basic Research Program of Shanxi Province (201901D211064), the National Natural Science Foundation of China (Grant 21706171, U1810204, No. 21978193), the Key Research and Development Program of Shanxi Province (20181102005, 201803D121120, 201805D131004). The theoretical calculations in this work were supported by Prof. Baojun Wang from State Key Laboratory of Clean and Efficient Coal Utilization, Taiyuan University of Technology.

Conflict of Interest

The authors declare no conflict of interest.

Keywords: Binary electrocatalyst · Li–S battery · Light-weight · Multifunction

- [1] H. Wu, Y. Li, J. Ren, D. Rao, Q. Zheng, L. Zhou, D. Lin, *Nano Energy* **2019**, 55, 82–92.
- [2] Y. Zhao, Y. Ye, F. Wu, Y. Li, L. Li, R. Chen, *Adv. Mater.* **2019**, 31, 1–27.
- [3] Z. Wang, J. Shen, J. Liu, X. Xu, Z. Liu, R. Hu, L. Yang, Y. Feng, J. Liu, Z. Shi, L. Ouyang, Y. Yu, M. Zhu, *Adv. Mater.* **2019**, 31, 1–11.
- [4] Y. Huang, W. Wang, J. Shan, J. Zhu, S. Wu, F. Li, Z. Liu, Y. Li, *Chem. Eng. J.* **2020**, 401, 126076.
- [5] W. G. Lim, Y. D. Mum, A. Cho, *ACS Nano* **2018**, 12, 6013–6022.
- [6] W. G. Lim, S. Kim, C. Jo, *Angew. Chem. Int. Ed.* **2019**, 58, 18746–18757; *Angew. Chem.* **2019**, 131, 18920–18931.
- [7] Z. Bian, Y. Xu, T. Yuan, C. Peng, Y. Pang, J. Yang, *Batteries & Supercaps* **2019**, 2, 560.
- [8] T. Boenke, P. Härtel, S. Dörfler, T. Abendroth, *Batteries & Supercaps* **2021**, 4, 989.
- [9] D. Guo, F. Ming, H. Su, Y. Wu, W. Wahyudi, M. Li, M. N. Hedhili, G. Sheng, L. J. Li, H. N. Alshareef, Y. Li, Z. Lai, *Nano Energy* **2019**, 61, 478–485.
- [10] C. Xian, P. Jing, X. Pu, G. Wang, Q. Wang, H. Wu, Y. Zhang, *ACS Appl. Mater. Interfaces* **2020**, 12, 47599–47611.
- [11] X. Hong, Y. Liu, J. Fu, X. Wang, T. Zhang, S. Wang, F. Hou, J. Liang, *Carbon* **2020**, 170, 119–126.
- [12] H. Shi, Z. Sun, W. Lv, S. Wang, Y. Shi, Y. Zhang, S. Xiao, H. Yang, Q. H. Yang, F. Li, *J. Mater. Chem. A* **2019**, 7, 11298–11304.
- [13] H. J. Shih, J. Y. Chang, C. S. Cho, C. C. Li, *Carbon* **2020**, 159, 401–411.
- [14] L. Zhang, Y. Wang, Z. Niu, J. Chen, *Carbon* **2019**, 141, 400–416.
- [15] M. A. Weret, C. F. Jeffrey Kuo, T. S. Zeleke, T. T. Beyene, M. C. Tsai, C. J. Huang, G. B. Berhe, W. N. Su, B. J. Hwang, *Energy Storage Mater.* **2020**, 26, 483–493.
- [16] H. Hu, Y. Hu, H. Cheng, S. Dai, K. Song, M. Liu, *J. Power Sources* **2021**, 491, 229617.
- [17] J. H. Park, W. Y. Choi, J. Yang, D. Kim, H. Gim, J. W. Lee, *Carbon* **2021**, 172, 624–636.
- [18] Q. Xiao, G. Li, M. Li, R. Liu, H. Li, P. Ren, Y. Dong, M. Feng, Z. Chen, *J. Energy Chem.* **2020**, 44, 61–67.
- [19] D. Fang, G. Wang, S. Huang, T. Chen, J. Yu, *Chem. Eng. J.* **2021**, 411, 128546.
- [20] X. Liu, Q. He, H. Yuan, C. Yan, Y. Zhao, X. Xu, J. Huang, *J. Energy Chem.* **2020**, 48, 109–115.
- [21] Y. Yu, Y. Zhang, L. Shu, Y. Li, Y. Wang, *J. Energy Chem.* **2020**, 49, 339–347.
- [22] B. Liu, M. Taheri, J. F. Torres, Z. Fusco, Y. Liu, T. Suzuki, G. Yu, A. Tricoli, *ACS Nano* **2020**, 14, 13852–13864.
- [23] M. Li, X. Zhou, X. Ma, L. Chen, D. Zhang, S. Xu, D. Duan, C. Chen, Q. Yuan, S. Liu, *Chem. Eng. J.* **2021**, 409, 128164.
- [24] S. Seo, S. Yu, S. Park, D. Kim, *Small* **2020**, 2004806, 1–13.
- [25] X. Yang, S. Chen, W. Gong, X. Meng, J. Ma, J. Zhang, L. Zheng, H. D. Abruna, J. Geng, *Small* **2020**, 2004950, 1–10.
- [26] G. Xia, J. Ye, Z. Zheng, X. Li, C. Chen, C. Hu, *Carbon* **2021**, 172, 96–105.
- [27] T. Liu, Y. Zhang, C. H. Li, M. D. Marquez, H. V. Tran, F. C. Robles Hernández, Y. Yao, T. R. Lee, *ACS Appl. Mater. Interfaces* **2020**, 12, 47368–47376.
- [28] M. Wang, S. Tan, S. Kan, Y. Wu, S. Sang, K. Liu, H. Liu, *J. Energy Chem.* **2020**, 49, 316–322.
- [29] P. Wang, B. Xi, M. Huang, W. Chen, J. Feng, S. Xiong, *Adv. Energy Mater.* **2021**, 2002893, 1–34.
- [30] X. Tao, J. Wan, C. Liu, H. Wang, H. Yao, G. Zheng, Z. W. Seh, Q. Cai, W. Li, G. Zhou, C. Zu, Y. Cui, *Nat. Commun.* **2016**, 7, 11203.
- [31] J. He, G. Hartmann, M. Lee, G. S. Hwang, Y. Chen, A. Manthiram, *Energy Environ. Sci.* **2019**, 12, 344–350.
- [32] X. Wang, D. Luo, J. Wang, Z. Sun, G. Cui, Y. Chen, T. Wang, L. Zheng, Y. Zhao, L. Shui, G. Zhou, K. Kempa, Y. Zhang, Z. Chen, *Angew. Chem. Int. Ed.* **2021**, 60, 2371–2378; *Angew. Chem.* **2021**, 133, 2401–2408.
- [33] H. Chen, G. Ke, X. Wu, W. Li, Y. Li, H. Mi, L. Sun, Q. Zhang, C. He, X. Ren, *Chem. Eng. J.* **2021**, 406, 126775.

- [34] M. E. Pam, S. Huang, S. Fan, D. Geng, D. Kong, S. Chen, M. Ding, L. Guo, L. K. Ang, H. Y. Yang, *Mater. Today* **2020**, *16*, 100380.
- [35] W. Lim, C. Jo, A. Cho, J. Hwang, S. Kim, J. W. Han, J. Lee, *Adv. Mater.* **2019**, *1806547*, 1–9.
- [36] Z. Sun, J. Zhang, L. Yin, G. Hu, R. Fang, H. Cheng, F. Li, *Nat. Publ. Gr.* **2017**, *8*, 14627.
- [37] J. Li, W. Xie, S. Zhang, S. Xu, M. Shao, *J. Mater. Chem. A* **2021**, *9*, 11151–11159.
- [38] F. Zeng, Z. Jin, K. Yuan, S. Liu, X. Cheng, A. Wang, W. Wang, Y. S. Yang, *J. Mater. Chem. A* **2016**, *4*, 12319–12327.
- [39] Y. Cui, Q. Zhang, J. Wu, X. Liang, A. P. Baker, D. Qu, H. Zhang, H. Zhang, X. Zhang, *J. Power Sources* **2018**, *378*, 40–47.
- [40] L. Ma, H. L. Zhuang, S. Wei, K. E. Hendrickson, M. S. Kim, G. Cohn, R. G. Hennig, L. A. Archer, *ACS Nano* **2016**, *10*, 1050–1059.
- [41] H. Hareendrakrishnakumar, R. Chulliyote, M. G. Joseph, S. Suriyakumar, A. M. Stephan, *Electrochim. Acta* **2019**, *321*, 134697.
- [42] S. J. Fretz, U. Pal, G. M. A. Girard, P. C. Howlett, A. E. C. Palmqvist, *Adv. Funct. Mater.* **2020**, *30*, 2002485.
- [43] D. Wang, F. Li, R. Lian, J. Xu, D. Kan, Y. Liu, G. Chen, Y. Gogotsi, Y. Wei, *ACS Nano* **2019**, *13*, 11078–11086.
- [44] J. Sun, J. Hwang, P. Jankowski, L. Xiao, J. S. Sanchez, Z. Xia, S. Lee, A. V. Talyzin, A. Matic, V. Palermo, Y. Sun, M. Agostini, *Small* **2021**, *17*, 2007242.
- [45] Z. Jia, H. Zhang, Y. Yu, Y. Chen, J. Yan, *J. Energy Chem.* **2020**, *43*, 71–77.
- [46] R. Mo, D. Rooney, K. Sun, *Energy Storage Mater.* **2020**, *26*, 414–422.
- [47] S. Chen, X. Han, J. Luo, J. Liao, J. Wang, Q. Deng, Z. Zeng, S. Deng, *Chem. Eng. J.* **2019**, *385*, 123457.
- [48] K. Yang, L. Zhong, Y. Mo, R. Wen, M. Xiao, D. Han, S. Wang, Y. Meng, *ACS Appl. Energ. Mater.* **2018**, *1*, 2555–2564.
- [49] A. Shukla, P. Dhanasekaran, S. Sasikala, N. Nagaraju, S. D. Bhat, V. K. Pillai, *J. Membr. Sci.* **2020**, *595*, 117484.
- [50] F. Zeng, Z. Jin, K. Yuan, S. Liu, X. Cheng, A. Wang, W. Wang, Y. Yang, *2016*, *4*, 12319–12327.
- [51] Y. Pang, J. Wei, Y. Wang, Y. Xia, *Adv. Energy Mater.* **2018**, *8*, 1–11.
- [52] Y. Zhang, P. Zhang, B. Li, S. Zhang, K. Liu, R. Hou, X. Zhang, S. R. P. Silva, G. Shao, *Energy Storage Mater.* **2020**, *27*, 159–168.
- [53] Y. Lei, C. Xiong, L. Dong, H. Guo, X. Su, J. Yao, Y. You, D. Tian, X. Shang, *Small* **2007**, *3*, 1889–1893.
- [54] X. Fu, F. Dunne, M. Chen, W. H. Zhong, *Nanoscale* **2020**, *12*, 5483–5493.
- [55] F. L. Zeng, X. Y. Zhou, N. Li, A. B. Wang, W. K. Wang, Z. Q. Jin, Y. R. Ren, B. J. Fang, N. Y. Yuan, J. N. Ding, *Energy Storage Mater.* **2021**, *34*, 755–767.
- [56] Z. Fang, Y. Luo, H. Wu, L. Yan, F. Zhao, Q. Li, S. Fan, J. Wang, *Carbon* **2020**, *166*, 183–192.
- [57] C. S. Cho, J. Y. Chang, C. C. Li, *J. Power Sources* **2020**, *451*, 227818.
- [58] J. Li, Y. Chen, S. Zhang, W. Xie, S. M. Xu, G. Wang, M. Shao, *ACS Appl. Mater. Interfaces* **2020**, *12*, 49519–49529.
- [59] S. Zhou, S. Yang, X. Ding, Y. Lai, H. Nie, Y. Zhang, D. Chan, H. Duan, S. Huang, Z. Yang, *ACS Nano* **2020**, *14*, 0c03403.
- [60] J. Cai, J. Jin, Z. Fan, C. Li, Z. Shi, J. Sun, Z. Liu, *Adv. Mater.* **2020**, *2005967*, 1–9.
- [61] Y. Qiu, L. Fan, M. Wang, X. Yin, X. Wu, X. Sun, D. Tian, B. Guan, D. Tang, N. Zhang, *ACS Nano* **2020**, *14*, 16105–16113.
- [62] B. Wang, F. Jin, Y. Xie, H. Luo, F. Wang, T. Ruan, D. Wang, Y. Zhou, S. Dou, *Energy Storage Mater.* **2020**, *26*, 433–442.
- [63] Z. Tong, L. Huang, H. Liu, W. Lei, H. Zhang, S. Zhang, Q. Jia, *Adv. Funct. Mater.* **2021**, *2010455*, 1–10.
- [64] J. Wang, L. Jia, H. Liu, C. Wang, J. Zhong, Q. Xiao, J. Yang, S. Duan, K. Feng, N. Liu, W. Duan, H. Lin, Y. Zhang, *ACS Appl. Mater. Interfaces* **2020**, *12*, 12727.
- [65] M. Zheng, X. Cai, Y. Tan, W. Wang, D. Wang, H. Fei, P. Saha, G. Wang, *Chem. Eng. J.* **2020**, *389*, 124404.
- [66] J. Kim, H. Shin, D. Yoo, S. Kang, S. Chung, K. Char, J. W. Choi, *Adv. Funct. Mater.* **2021**, *2106679*, 1–11.
- [67] T. Zhang, F. Hu, W. Shao, S. Liu, H. Peng, Z. Song, C. Song, N. Li, X. Jian, *ACS Nano* **2021**, *15*, 15027–15038.
- [68] L. Fang, Z. Feng, L. Cheng, R. E. Winans, T. Li, *Small Methods* **2020**, *4*, 1–17.
- [69] J. W. Kim, G. Seo, S. Bong, J. Lee, *ChemSusChem* **2020**, *14*, 876–883.
- [70] X. Wang, W. Zhang, D. Wang, H. L. Zhuang, S. Li, L. Fan, LinlinLi, X. Wang, Y. He, Y. Lu, *Energy Storage Mater.* **2020**, *26*, 378–384.
- [71] W. Mao, W. Yue, Z. Xu, S. Chang, Q. Hu, F. Pei, X. Huang, J. Zhang, D. Li, G. Liu, G. Ai, *ACS Nano* **2020**, *14*, 4741–4754.
- [72] D. Guo, X. Li, W. Wahyudi, C. Li, A. H. Emwas, M. N. Hedhili, Y. Li, Z. Lai, *ACS Nano* **2020**, *14*, 17163–17173.
- [73] P. Qiu, Y. Yao, W. Li, Y. Sun, Z. Jiang, B. Mei, L. Gu, Q. Zhang, T. Shang, X. Yu, J. Yang, Y. Fang, G. Zhu, Z. Zhang, X. Zhu, T. Zhao, W. Jiang, Y. Fan, L. Wang, B. Ma, L. Liu, Y. Yu, W. Luo, *Nano Lett.* **2021**, *21*, 700–708.
- [74] D. Yang, C. Zhang, J. J. Biendicho, X. Han, Z. Liang, R. Du, M. Li, J. Li, J. Arbiol, J. Llorca, Y. Zhou, J. R. Morante, A. Cabot, *ACS Nano* **2020**, *14*, 15492–15504.
- [75] X. Fan, R. Yuan, J. Lei, X. Lin, P. Xu, X. Cui, L. Cao, M. Zheng, Q. Dong, *ACS Nano* **2020**, *14*, 15884–15893.
- [76] Y. Liu, M. Chen, Z. Su, Y. Gao, Y. Zhang, D. Long, *Carbon* **2021**, *172*, 260–271.
- [77] J. Xu, Q. Zhang, X. Liang, J. Yan, J. Liu, Y. Wu, *Nanoscale* **2020**, *12*, 6832–6843.
- [78] Z. Xiao, Z. Li, P. Li, X. Meng, R. Wang, *Nano Energy* **2020**, *70*, 104522.

Manuscript received: October 14, 2021

Revised manuscript received: November 18, 2021

Accepted manuscript online: November 19, 2021

Version of record online: December 6, 2021